

In-Situ Observations of Phase Transformations in the HAZ of 2205 Duplex Stainless Steel Weldments

T. A. Palmer, J. W. Elmer, J. Wong

This article was submitted to
International Conference on Joining of Advanced and Specialty
Materials IV, 2001 ASM Materials Solutions Conference and
Exposition, Indianapolis, IN, November 5-8, 2001

U.S. Department of Energy

Lawrence
Livermore
National
Laboratory

August 15, 2001

DISCLAIMER

This document was prepared as an account of work sponsored by an agency of the United States Government. Neither the United States Government nor the University of California nor any of their employees, makes any warranty, express or implied, or assumes any legal liability or responsibility for the accuracy, completeness, or usefulness of any information, apparatus, product, or process disclosed, or represents that its use would not infringe privately owned rights. Reference herein to any specific commercial product, process, or service by trade name, trademark, manufacturer, or otherwise, does not necessarily constitute or imply its endorsement, recommendation, or favoring by the United States Government or the University of California. The views and opinions of authors expressed herein do not necessarily state or reflect those of the United States Government or the University of California, and shall not be used for advertising or product endorsement purposes.

This is a preprint of a paper intended for publication in a journal or proceedings. Since changes may be made before publication, this preprint is made available with the understanding that it will not be cited or reproduced without the permission of the author.

This work was performed under the auspices of the United States Department of Energy by the University of California, Lawrence Livermore National Laboratory under contract No. W-7405-Eng-48.

This report has been reproduced directly from the best available copy.

Available electronically at <http://www.doc.gov/bridge>

Available for a processing fee to U.S. Department of Energy
And its contractors in paper from
U.S. Department of Energy
Office of Scientific and Technical Information
P.O. Box 62
Oak Ridge, TN 37831-0062
Telephone: (865) 576-8401
Facsimile: (865) 576-5728
E-mail: reports@adonis.osti.gov

Available for the sale to the public from
U.S. Department of Commerce
National Technical Information Service
5285 Port Royal Road
Springfield, VA 22161
Telephone: (800) 553-6847
Facsimile: (703) 605-6900
E-mail: orders@ntis.fedworld.gov
Online ordering: <http://www.ntis.gov/ordering.htm>

OR

Lawrence Livermore National Laboratory
Technical Information Department's Digital Library
<http://www.llnl.gov/tid/Library.html>

In-Situ Observations of Phase Transformations in the HAZ of 2205 Duplex Stainless Steel Weldments

T.A. Palmer, J.W. Elmer, and Joe Wong
Lawrence Livermore National Laboratory

Ferrite (δ)/austenite (γ) transformations in the heat affected zone (HAZ) of a gas tungsten arc (GTA) weld in 2205 duplex stainless steel are observed in real-time using spatially resolved X-ray diffraction (SRXRD) with high intensity synchrotron radiation. A map showing the locations of the δ and γ phases with respect to the calculated weld pool dimensions has been constructed from a series of SRXRD scans. Regions of liquid, completely transformed γ , a combination of partially transformed γ with untransformed δ , and untransformed $\delta+\gamma$ are identified. Analysis of each SRXRD pattern provides a semi-quantitative definition of both the δ/γ phase balance and the extent of annealing which are mapped for the first time with respect to the calculated weld pool size and shape. A combination of these analyses provides a unique real-time description of the progression of phase transformations in the HAZ. Using these real-time observations, important kinetic information about the transformations occurring in duplex stainless steels during heating and cooling cycles typical of welding can be determined.

Introduction

Duplex stainless steels (DSS) have a mixed microstructure characterized by elongated austenite (γ -fcc) grains in a ferrite (δ -bcc) matrix. They are processed, usually by hot working or annealing in the two phase ($\delta+\gamma$) region, to produce a balance between the amount of δ and γ in the finished product. With this microstructure, duplex stainless steels combine the desirable properties common to both austenitic and ferritic steels. For example, duplex steels typically display a yield strength about double that of a typical austenitic steel with a superior resistance to stress corrosion cracking approaching that of a ferritic stainless steel and the ease of fabricability of an austenitic steel. The combination of these desirable properties makes them an important class of engineering materials, with a variety of applications in the marine and petrochemical fields and beyond.¹⁻⁷

During fusion welding processes, the base metal microstructure is altered in both the heat affected zone (HAZ) and the fusion zone. In the fusion zone, duplex stainless steels solidify entirely as δ .⁴ Once solidified, the high-temperature

ferrite can undergo a solid-state phase transformation to austenite with sufficient cooling. Even though temperatures in the HAZ do not exceed the liquidus temperature and no solidification during the cooling cycle occurs, phase transformations in the HAZ are equally complicated. For example, the heating and cooling cycles prevalent in the HAZ drive the δ/γ phase transformation in different ways, depending on the location, and create a non-homogenous structure.³⁻¹⁰

Several researchers have specifically investigated the δ/γ phase transformation in the HAZ of various DSSs during a number of different fusion welding processes.⁸⁻¹³ They have collectively identified a number of features of this phase transformation. For example, the heating cycle is dominated by the transformation of γ into δ and the growth of the ferrite grains. The cooling cycle is dominated by the transformation of δ into γ . Other processes driven by the weld thermal cycles, such as alloy element partitioning, are also observed and found to affect the δ/γ transformation. Even though a number of different welding processes over a range of different welding parameters have been examined, the conclusions are based on either empirical models or theoretical analyses based on thermodynamics and transformation kinetic theory. Direct observation of these phase transformations in real-time is required for more realistic input into these models and to gain a better understanding of the phase transformations in this material system.

Spatially resolved x-ray diffraction (SRXRD) with high intensity x-rays produced by synchrotron radiation has recently been developed and used to study HAZ phase transformations in GTA welds.¹⁴⁻²¹ This technique allows the phase transformations to be directly observed in real-time with high spatial resolution during both the heating and cooling cycles of the welding process. Several materials systems have been studied using this technique, including commercially pure titanium,¹⁴⁻¹⁷ plain carbon steel (AISI 1005),¹⁸ austenitic stainless steel (AISI 304),¹⁹⁻²⁰ and flux core arc welding (FCAW) filler metals.²¹ Prominent phase transformations specific to each alloy have been mapped, and significant insights into the associated kinetics of phase transformations in the HAZ of welds have been gained.

In this study, SRXRD is used to investigate the δ/γ transformation in the HAZ of a GTA weld in a 2205 DSS. A detailed map of the phases present in the HAZ using the SRXRD results is developed. Regions containing the liquid weld pool, completely transformed γ , a combination of untransformed δ and partially transformed γ , and untransformed γ and δ are identified. The locations of these phase regions are compared with the calculated temperature isotherms of particular importance to this alloy. Individual SRXRD patterns are also shown to provide semi-quantitative information about the transient volume fractions of the δ and γ phases during the welding. Furthermore, the width of the Bragg peaks provides a means of detecting the effects of annealing of the phases within the HAZ. Based on these results, characteristics of the phase transformations occurring within the HAZ and the metal affected by the welding process are determined using direct real-time observations.

Experimental

Material and Welding Parameters

A series of gas tungsten arc (GTA) welding experiments have been performed on a 2205 DSS (22.43 Cr-4.88 Ni-3.13 Mo-1.40 Mn-0.023 C-0.18 N-0.004 S-0.005 O-0.0007H-0.67 Si-0.02 Al-0.03 B-0.08 Co-0.20 Cu-0.03 Nb-0.028 P->0.005 Ti-0.05 V- Bal. Fe). The as-received material has been solution annealed at 1065°C for 2.5 hours followed by water quenching to ambient temperatures. Cylindrical welding samples (10.2 cm diameter, 8 cm long) have been machined from the as-received forged bar stock.

GTA welds are made using a peak current of 130 A and a background current of 90 A pulsed at a frequency of 300 Hz. The pulsing parameters are designed to minimize the side-to-side motion of the liquid weld pool, thus decreasing the potential experimental error in the location of the liquid/solid interface. The arc gap is set at a distance of 0.28 cm, correlating to an arc voltage of 17 V, and welding was performed using a W-2% Th electrode with a diameter of 0.47 cm. Shielding is provided to the weld pool by high-purity (99.999%) helium being flowed through the torch and from a helium side blow, which removes soot (condensed metal vapors) from the area being examined with the synchrotron x-rays. A travel speed of 0.6 mm/sec is achieved by rotating the cylindrical bar at a constant speed of 0.11 rpm below a stationary electrode. A new electrode is used for each weld and is straight ground with a 90° included angle taper.

To avoid contamination of the weld metal with the external atmosphere, welding is performed in an environmentally sealed chamber. The welding process is monitored with an infrared (IR) camera (Inframetrics, Inc. Model 600). This camera has a 0.46 m focal length and a 40 x 25 mm field of view. Prior to welding, the chamber is evacuated to a vacuum level of approximately 8 Pa using a mechanical roughing pump, after which the chamber is backfilled with helium until it reaches atmospheric pressure.

The microstructures of the 2205 DSS base metal and the weldment have been examined using optical microscopy. Etching of the samples is performed using an electrolytic

NaOH etch described in ASTM standard A 923-98.²² A Nikon EpiPhot metallurgical microscope, outfitted with a Polaroid Digital Microscope Camera, is used in performing the optical metallography. The typical base metal microstructure of the 2205 DSS studied here is shown in Figure 1. A two phase δ/γ structure is shown, in which the darker phase is ferrite and the lighter phase is austenite.

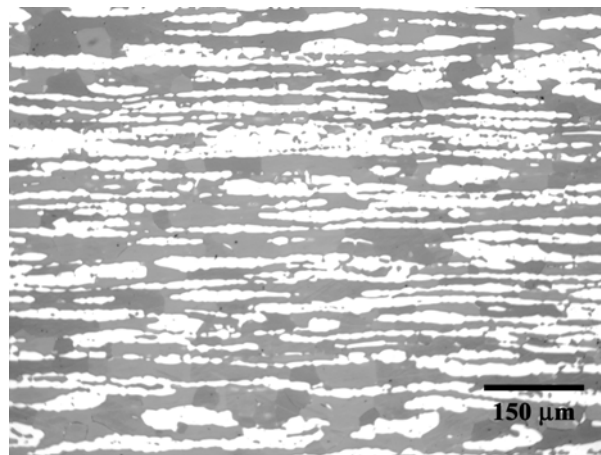


Figure 1. Optical micrograph of typical base metal microstructure in the 2205 DSS: austenite: light; ferrite: dark.

The volume fractions of the ferrite phase in the base metal are measured using Scion Image (Scion Corporation). These measurements have been used as a standard to convert the intensity fraction measurements in the SRXRD results to the suitable volume fractions. In addition, microhardness measurements (Vickers' hardness scale) have also been made across the top surface of the weldment at 0.25 mm intervals and a load of 50 gm.

SRXRD Parameters

The SRXRD experiments are performed on the 31-pole wiggler beam line (BL 10-2)²³ at the Stanford Synchrotron Radiation Laboratory (SSRL) on the Stanford Positron-Electron Asymmetric Ring (SPEAR).¹⁴⁻²¹ In this setup, the synchrotron beam emerges from the wiggler and is focused by a toroidal mirror to a size of approximately 1 mm high x 2 mm wide and monochromatized with a double Si(111) crystal. The focused beam then passes through a 260 μ m tungsten pinhole to render a sub-millimeter beam on the sample at an incident angle of approximately 25°. These portions of the experimental set-up are shown schematically in Figure 2. A photon energy of 12.0 keV ($\lambda = 0.1033$ nm) has been chosen to maximize the number of observable diffraction peaks and to ensure that the photon energy is high enough above the Fe K-edge (7.112 keV) and the Ni K-edge (8.332 keV) to minimize the K-fluorescence contribution from the sample. Further details regarding the experimental set-up are described in detail elsewhere.¹⁴⁻²¹

In a typical SRXRD run, a total of 38 diffraction patterns spaced either 250 μ m or 500 μ m apart are gathered along a linear path outward from the weld centerline into the HAZ. The path covered by the SRXRD run spans between 10 and 20

mm, depending on the spacing between each data point. A diffraction pattern is recorded while the beam is at a fixed location with respect to the welding electrode. For each pattern, an integration time of 10 seconds is used while the bar is rotated under the torch at a constant speed. With a travel speed of 0.6 mm/sec, each SRXRD pattern is integrated over a distance of 6 mm. Within 2θ range examined here (approximately 25° to 57°), there are three peaks associated with the bcc (δ -Fe) and four peaks associated with the fcc (γ -Fe) phases in the 2205 DSS.²⁴

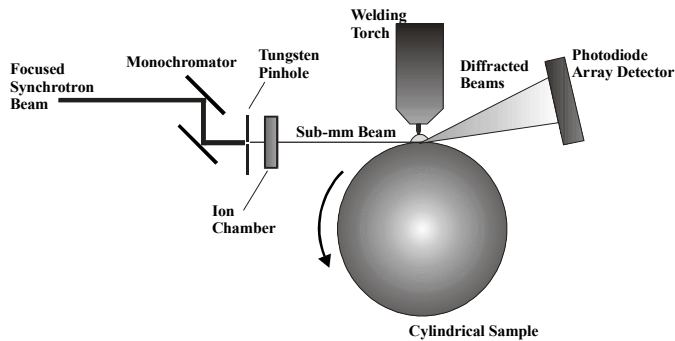


Figure 2. Schematic diagram of the SRXRD experimental setup.

Further analysis of the individual Bragg peaks in each SRXRD pattern is undertaken in order to extract the microstructural properties of various phases in the material at specific locations. Both the area under the peak and the full width at half maximum (FWHM) values are determined for each peak in every SRXRD pattern. In order to measure the area and width of a given peak, the experimental peak is fitted with a sum of one or more Gaussian peak profile functions and a linear background.¹⁶ The area and FWHM values of the fitted Gaussian functions are then measured using an automated curve-fitting routine developed in Igor Pro®, Version 3.1.²⁵

Modeling of Turbulent Heat Transfer and Fluid Flow

Knowledge of both the weld pool geometry and thermal cycles in the weldment is necessary to fully understand and map the phases present. Since the direct measurement of these properties is difficult, calculations using complex mathematical models have been undertaken.^{26,27} This model has been tested extensively on a number of different materials systems and welding parameters by DebRoy and coworkers.²⁶⁻³¹ Detailed descriptions of this model are available elsewhere,^{17,29,30} and only a cursory description is included below.

A three dimensional, turbulent heat transfer and fluid flow model numerically solves the equations of conservation of mass, momentum, and energy. In order to take into account the transient nature of welding, it is transformed into a steady-state problem by solving these equations in a coordinate system attached to and moving with the heat source. Components of the K- ϵ model, where K is the turbulent kinetic energy and ϵ is the dissipation rate of turbulent kinetic energy, are incorporated in order to solve the turbulent components of heat transfer and fluid flow.^{17,29,30} Within this model, the ef-

fects of turbulence on fluid flow and heat transfer in the weldment are included through the use of effective viscosity and effective thermal conductivity parameters, which are the sums of the turbulent and molecular components of each parameter. The value of the turbulent viscosity can be determined through the solution of the equations of conservation of K and ϵ . The turbulent thermal conductivity is then related to the turbulent viscosity by the turbulent Prandtl number, which is set to a value of 0.9.

The governing equations are represented by a set of finite difference equations and solved iteratively on a line by line basis utilizing a tri-diagonal matrix algorithm.^{17,29-31} The solution domain has dimensions of 30.7 cm in length, 5.3 cm in width, and 2.3 cm in thickness. A 56 x 40 x 32 grid system is used in the calculations. The boundary conditions used in these calculations^{17,29-31} are similar to those used in previous studies. For example, calculations have been performed in a Cartesian coordinate system on only half the workpiece because of the mirror symmetry of the weld pool, and a flat weld pool surface has been assumed. The data used in these calculations are listed in Table 1.^{28,32,33}

Table 1. Summary of material properties used in the heat transfer and fluid flow calculations.

Property	Value	Reference
Liquidus Temperature (K)	1715	
Solidus Temperature (K)	1589	
Density of Liquid (kg/m ³)	7200	32*
Enthalpy of Solid at Melting Point (J/kg)	1.05x10 ⁶	33
Enthalpy of Liquid at Melting Point (J/kg)	1.32x10 ⁶	33
Specific Heat of Solid (J/kg-K)	418.68	32
Specific Heat of Liquid (J/kg-K)	808.05	32
Thermal Conductivity of Solid (W/m-K)	18.83	32*
Thermal Conductivity of Liquid (W/m-K)	62.76	32*
Viscosity of Liquid (kg/m-sec)	0.006	32
Temperature Coefficient of Surface Tension (N/m-K)	-3.25x10 ⁻⁴	32*
Coefficient of Thermal Expansion (1/K)	1.00x10 ⁻⁵	32

* Values are based on approximations from pure metal values.

Values for the liquidus and solidus temperatures have been determined from a calculated pseudo-binary phase diagram³⁴ constructed using ThermoCalc®. Figure 3 shows the calculated mole fractions of the liquid, δ , and γ phases as a function of temperature. The role of each alloying element is taken into consideration when calculating the phase stability of the δ and γ phases, providing an increased accuracy in the calculation of the liquidus (1443°C), solidus (1316°C), and the δ/γ phase transformation (1316°C) temperatures. During cooling from the melt, these calculations predict that the mole

fraction of ferrite decreases with decreasing temperature, reaching a minimum value near 850°C. With further decreases in temperature, the ferrite mole fraction again increases, while the austenite mole fraction decreases.

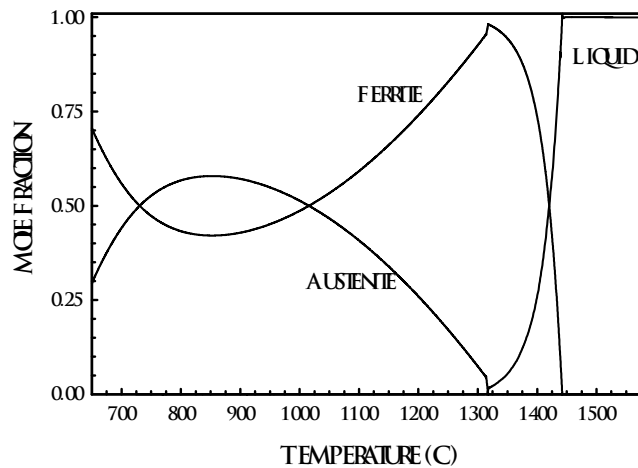


Figure 3. Calculated mole fractions of liquid, ferrite, and austenite in the 2205 DSS plotted as a function of temperature.²⁵

RESULTS AND DISCUSSION

SRXRD Results

Prior to each welding run, an initial room temperature x-ray scan of 10 seconds in duration is collected at the weld starting location. This scan provides an x-ray diffraction pattern characteristic of the base metal. There are four γ (fcc) and three δ (bcc) peaks visible, with the fcc (111) and bcc (110) peaks dominant. Texturing produces more intense (110) δ and (111) γ peaks in the base metal than in the calculated powder patterns.

Figures 4(a-d) show x-ray diffraction patterns gathered at several distances from the weld centerline at a location 1 mm ahead of the heat source. Changes in location produce changes in both the peaks present in each pattern and in their general characteristics. For example, the intensity, width, and 2θ position of each peak changes with the distance from the weld centerline. For example, at 3.75 mm from the weld centerline ($y=3.75$ mm) no peaks are present, indicating that this location is part of the liquid weld pool.

As the distance from the weld centerline increases to 4.75 mm ($y=4.75$ mm), only the bcc (110) peak is present. The presence of only a ferrite peak at this location indicates that

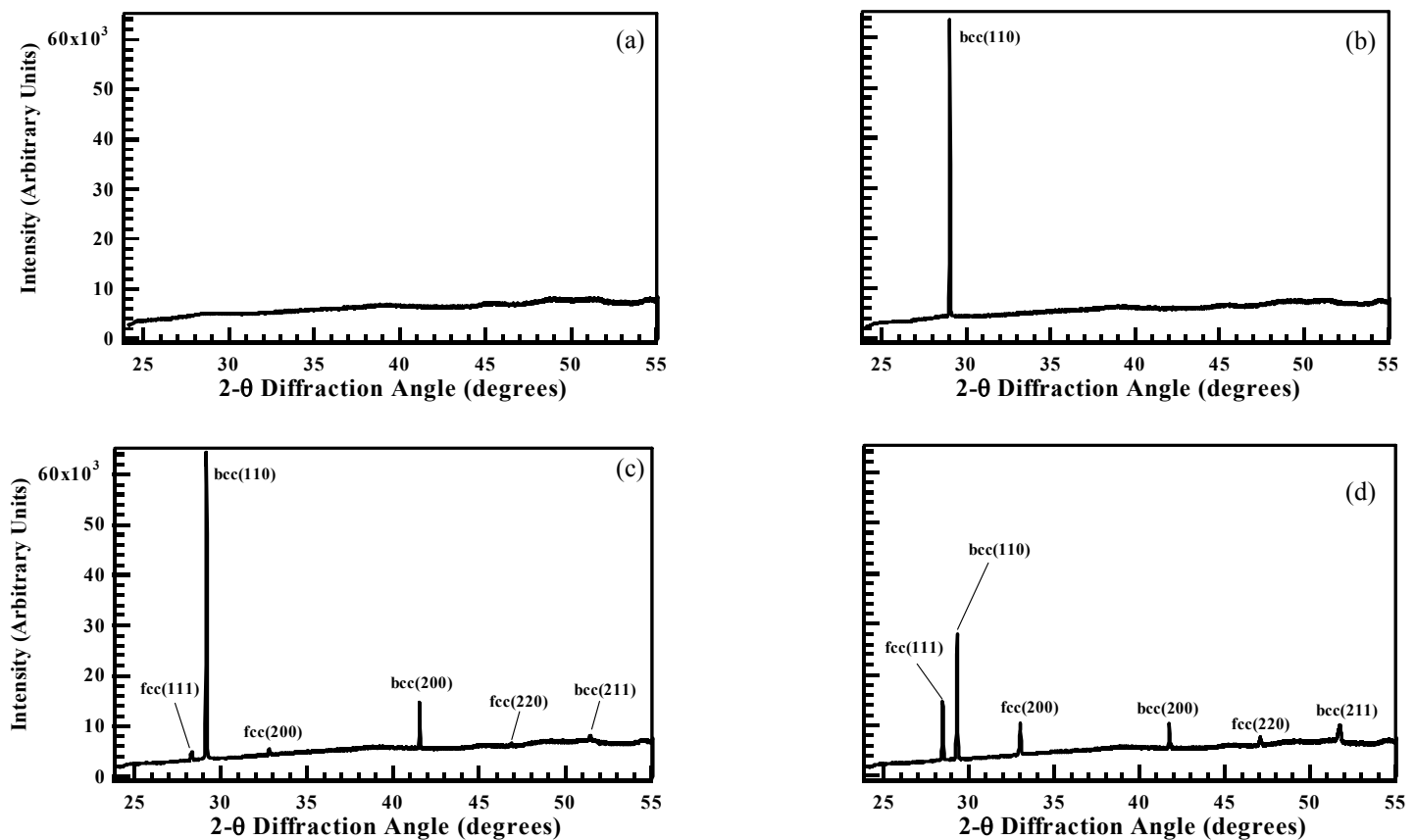


Figure 4(a-e). SRXRD patterns taken during welding at locations 1 mm ahead ($x=-1$ mm) of the electrode and at (a) $y = 3.75$ mm, (b) $y = 4.75$ mm, (c) $y = 5.50$ mm, and (d) $y = 6.75$ mm from the centerline of the weld pool.

complete transformation to ferrite has occurred. With further increases in the distance from the weld pool (Figures 4(c-d)), both ferrite and austenite peaks are present, but the general shape of each peak changes with location and the γ/δ ratio increases. These changes in the peak shape are related to the effects of the partial transformation and the annealing of the ferrite and austenite phases. Based on a collection of these sets of x-ray diffraction patterns, a map of the phases surrounding the weld pool can be constructed.

Modeling of Weld Pool Size and Shape

Along with the phase locations in the weldment, the weld pool shape and size and associated isotherms are calculated. Figure 5 shows the calculated steady-state temperature and fluid flow fields in the weld pool in three dimensions. Both the liquidus and solidus isotherms, which match the liquid/solid boundary and the δ/γ transformation temperature, respectively, are shown along with several additional isotherms in the liquid weld pool.

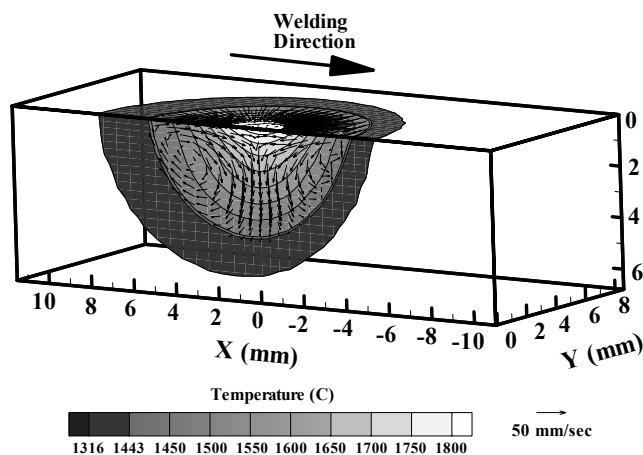


Figure 5. Three dimensional plot of results of the heat transfer and fluid flow calculations.

The general shape of the weld pool and characteristics of the velocity and temperature fields in this figure are character-

istic of welds made under these conditions. For example, the top surface of the weld pool displays only a slightly elongated shape, consistent with the rather slow travel speed used in these experiments. In addition, the downward direction of the velocity fields in the center of the weld pool is consistent with what would be expected with the presence of sulfur (0.004 wt. pct.).^{31,35,36} A comparison between the calculated and experimental weld pool cross sections is shown in Figure 6. Both cross sections display a similar shape, depth, and width, thereby, the calculated weld pool dimensions are adequately correlated with the experimental results for these weld conditions.

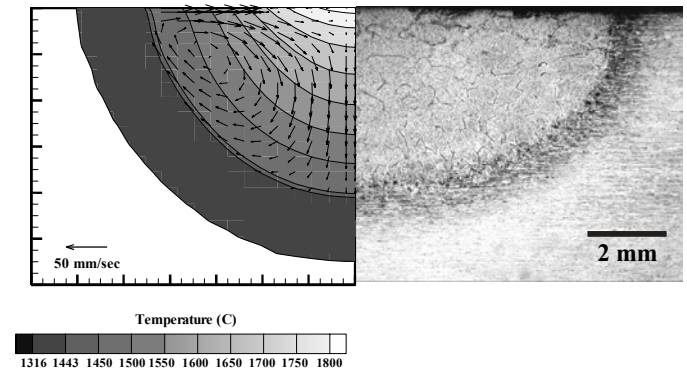


Figure 6. Comparison between the experimental and calculated weld pool cross sections.

SRXRD Phase Mapping

A detailed map of the locations of the γ and δ phases in the HAZ with respect to the calculated weld pool temperature, profiles is shown in Figure 7. Three primary phase regions (liquid, δ , and $\delta+\gamma$) are superimposed over the calculated liquidus (1443°C) and the δ/γ solvus (1316°C) isotherms. The liquidus isotherm (1443°C) very closely corresponds with the liquid phase locations in the SRXRD experiments. Adjacent to the liquid phase, the single phase ferrite region is observed.

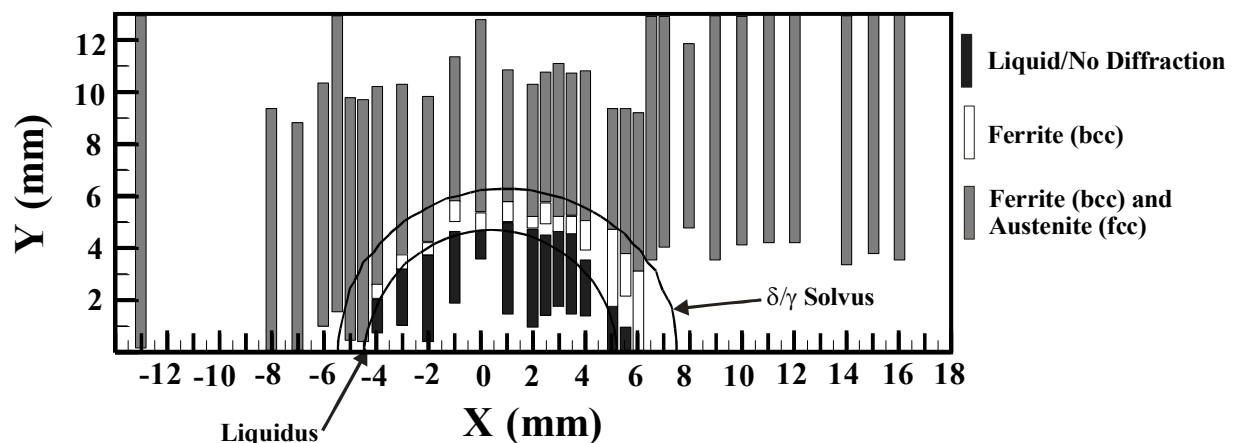


Figure 7. Complete phase map of the DSS weldment based on SRXRD observations and heat transfer and fluid flow calculations.

As the distance from the weld centerline increases, a two phase δ/γ region is observed adjacent to the single phase δ region and extends in all directions.

Each region identified in Figure 7 can be correlated with the temperatures experienced there. In the single phase δ region, the temperatures and times are sufficient to drive the complete transformation of the γ in the base metal duplex microstructure to δ . Based on thermodynamic calculations, the entire region between the liquidus and δ/γ solvus isotherms should consist only of δ . The presence of γ in this region results from the insufficient combination of time and temperature necessary to completely transform the γ to δ . A more detailed analysis of the SRXRD data is required in order to determine this boundary between the partially transformed γ and the untransformed duplex microstructure.

Analysis of SRXRD Patterns

Volume Fractions of the δ and γ Phases

The δ/γ phase balance in the HAZ evolves during the heating and cooling cycles of the welding process. This phase balance at a specific location can be semi-quantitatively determined by measuring the areas of the individual ferrite and austenite peaks in each SRXRD pattern. The peak areas measured in each SRXRD pattern are converted into the intensity fractions of austenite and ferrite, which are defined as the ratio of the sum of the measured peak area for each phase to the total peak area in a single SRXRD pattern.

Intensity fractions measured in the base metal are compared with base metal volume fractions determined from quantitative metallography measurements.^{28,29} These techniques are commonly used to determine the δ/γ phase balance in these alloys and provide verification for the SRXRD values. According to the metallographic measurements, a δ/γ phase balance of approximately 57:43 exists in the base metal. This phase balance compares well with that expected for the heat treatment conditions used in the processing of the base metal. On the other hand, the uncorrected base metal SRXRD data display a δ/γ phase balance of approximately 62:38.

This lack of agreement results from differences in the structure factors associated with the Bragg peaks of the phases as well as differences in the physical density of the ferrite and austenite (68% packing efficiency for bcc vs. 72% packing efficiency for fcc). Since these factors specifically affect the SRXRD peak area measurements, the base metal SRXRD values are calibrated with the metallographic measurements in order to convert the SRXRD measurements into volume fractions. Based on the conversion, the calculated calibration constant for δ (0.909) and γ (1.144) are applied to the measured SRXRD peak intensity fractions to determine the volume fractions of each phase.

Figure 8 shows the δ and γ volume fractions with increasing distance from the weld centerline 2 mm ahead ($x=-2$ mm) of the heat source. Only δ is present in the region adjacent to the weld pool edge. As the distance increases, the δ volume fraction decreases until $y=6$ mm, where both the δ and γ volume fractions stabilize at values equivalent to the measured base metal volume fractions.

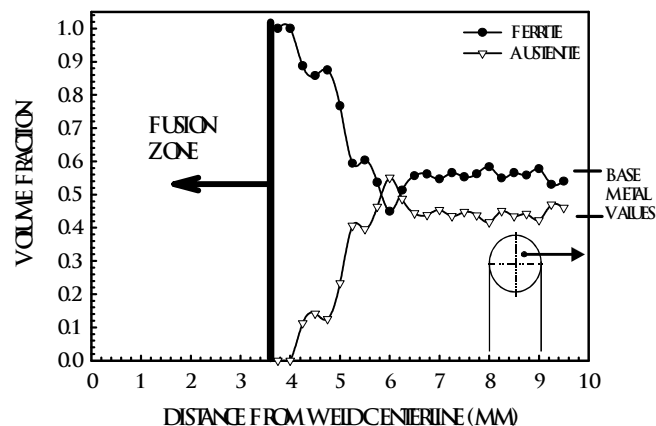


Figure 8. The δ/γ phase fractions measured from the SRXRD data are shown at 2 mm ahead ($x=-2$ mm) of the heat source.

A refined phase map, compiling all of these measurements is shown in Figure 9. This map tracks the progress of the δ/γ phase transformation during the welding process. Examination of this map shows that the δ volume fraction first decreases to levels below those found in the base metal on the leading edge of the weld pool. At locations behind the weld pool, the δ volume fraction rapidly recovers to that observed in the base metal.

In order to provide an explanation for this behavior, the thermal history and δ volume fraction are plotted as a function of location along a path parallel ($y=9.5$ mm) to the welding direction in Figure 10(a&b). During heating, the δ volume fraction decreases until a minimum value is reached near the peak temperature ($\sim 750^\circ\text{C}$). As the metal starts to cool, the δ volume fraction increases rather rapidly and approaches that observed in the base metal. These observations indicate that the $\delta \rightarrow \gamma$ phase transformation is favored during heating, up to temperatures approaching 750°C . Previous researchers have noted the possibility of the occurrence of the $\delta \rightarrow \gamma$ phase transformation in the HAZ only during the cooling cycle.^{8,9}

Thermodynamic calculations support the $\delta \rightarrow \gamma$ phase transformation on heating. An examination of Figure 3 shows that as the temperature increases from room temperature to approximately 850°C , the δ mole fraction decreases. The δ mole fraction reaches a minimum value in the vicinity of 850°C and increases with increasing temperature, reaching a value of 1.0 at a temperature of approximately 1316°C . The δ and γ volume fractions shown in Figure 10(b) are generally consistent with these thermodynamic calculations. While these thermodynamic calculations provide insight into the stability of δ and γ , they do not provide information about the kinetics of the $\delta \rightarrow \gamma \rightarrow \delta$ transformation on heating and cooling. Further work is required to more adequately understand the mechanisms underlying these observations.

Annealing

Measurement of the FWHM values of the γ and δ peaks can provide additional insight into the effects of the welding

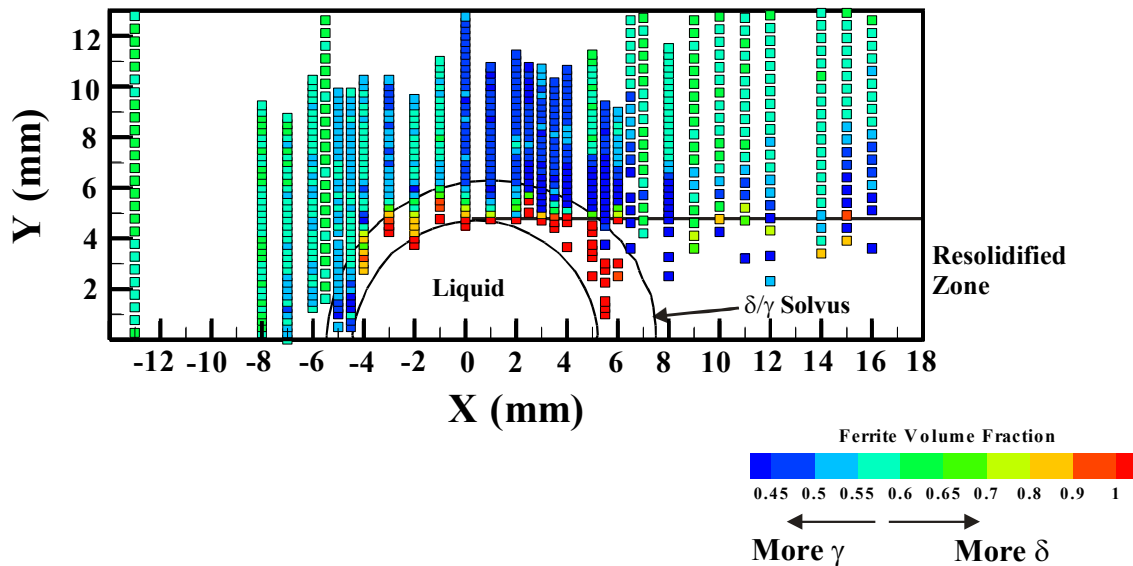


Figure 9. Phase map showing the ferrite volume fractions calculated from the SRXRD patterns.

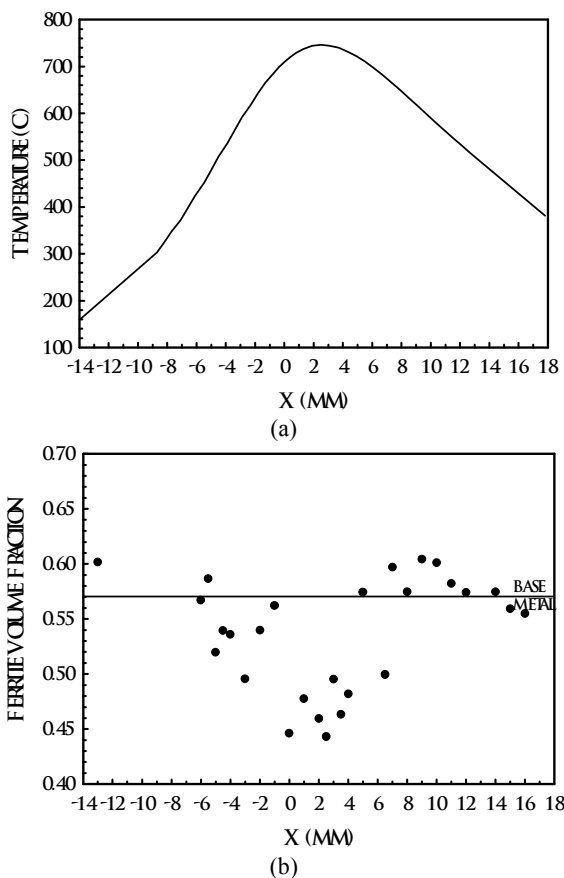


Figure 10(a&b). Variations in (a) temperature and (b) the δ volume fraction at 9.5 mm from the weld centerline ($y=9.5$ mm).

process on the material. Previous work¹¹⁻¹⁴ has noted a narrowing of the peak width from the base metal value with heating. These same peak narrowing effects are observed in the DSS and are illustrated here using the fcc (111) and bcc (110)

peaks. Peak widths are measured in each SRXRD pattern and compared with the appropriate base metal peak width. A ratio between these two values is then used as a measure of the effect of the thermal cycles on the material at that specific location. When this ratio reaches a value of 1.0, the base metal has been reached.

The FWHM ratios for the fcc (111) and bcc (110) peaks are plotted in Figure 11 as a function of the distance from the weld centerline at locations 5.5 mm ahead ($x=-5.5$ mm) of the heat source. These ratios increase with increasing distance from the weld centerline and reach base metal values at distances of nearly 10 mm ($y=10$ mm) from the weld centerline. The FWHM ratios for the δ and γ peaks are nearly identical, indicating that the two phases are affected by the annealing conditions in much the same fashion.

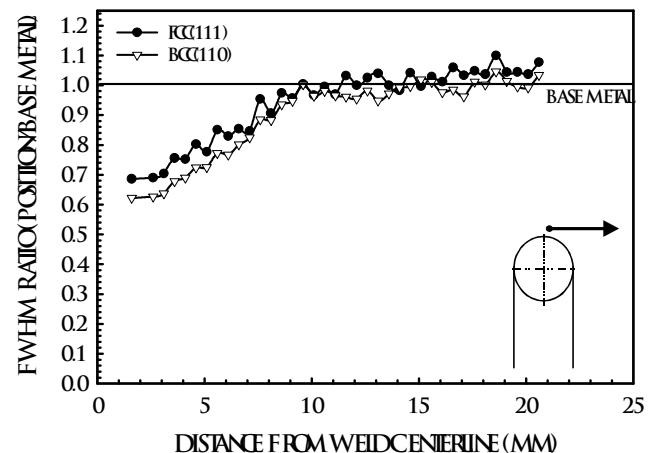


Figure 11. Plot showing the FWHM ratios of the fcc (111) and bcc(110) peaks at 5.5 mm ahead ($x=-5.5$ mm) of the heat source.

A map showing the locations where the FWHM ratios are at least 0.9 for the fcc (111) and bcc (110) peaks is shown in

Figure 12. It is assumed that a FWHM ratio of 0.9 generally corresponds to the boundary between the annealed material and the base metal. The FWHM ratios of both the δ and γ peaks reach this value at a distance of approximately 12 mm from the weld centerline. Behind the weld pool, the FWHM values retain the same distance from the weld pool edge as that established during the heating cycle.

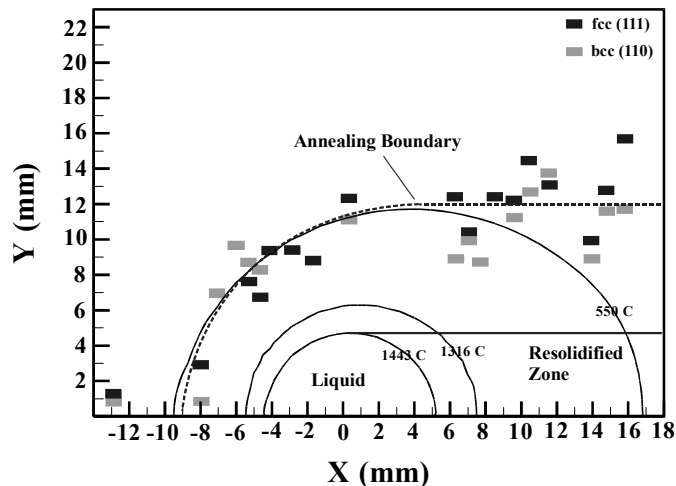


Figure 12. Phase map showing the locations at which the FWHM values of the fcc (111) and bcc (110) reach 0.9 of the base metal.

This boundary corresponds well with the 550°C isotherm. It can therefore be assumed that the effects of annealing in the weldment are observed at temperatures beginning around 550°C. Lower welding temperatures produce no observable change in the base metal. These calculations also show that the effects of the welding process, at least for the welding parameters analyzed here, extend to distances of approximately

12 mm from the weld centerline. This boundary between the annealed region and the base metal corresponds well with the results of microhardness measurements made across the fusion zone and HAZ.

Combined Map of HAZ

SRXRD results and those of the turbulent heat transfer and fluid flow model are combined in a schematic map shown in Figure 13. In this map, phase transformations and the regions over which they occur are identified. Several of the transformations identified here are observed only in real-time using SRXRD. No other means is available for observing these transformations since the evidence of these reactions disappears with the onset of cooling.

The weld heating and cooling cycles are the primary drivers for these phase transformations. For example, certain reactions (2-5) occur during heating, while others (7-10) are observed only during cooling. During heating, the material first experiences annealing (2) as temperatures exceed 550°C. After annealing, the material undergoes its first transformation, in which the δ in the duplex δ/γ base metal microstructure begins to transform to γ (3). This transformation, which begins at temperatures of approximately 700°C, accounts for the decreased δ volume fractions observed in Figures 9 and 10.

As the weld pool is approached and temperatures continue to increase, the HAZ microstructure is governed by the peak temperature experienced at a given location. At peak temperatures exceeding approximately 1100°C, γ begins to transform to δ (4). Increasing peak temperatures further drive this reaction. When the peak temperatures exceed approximately 1375°C, the remaining γ completely transforms to δ (5). With lower peak temperatures, the $\delta \rightarrow \gamma$ reaction (3)

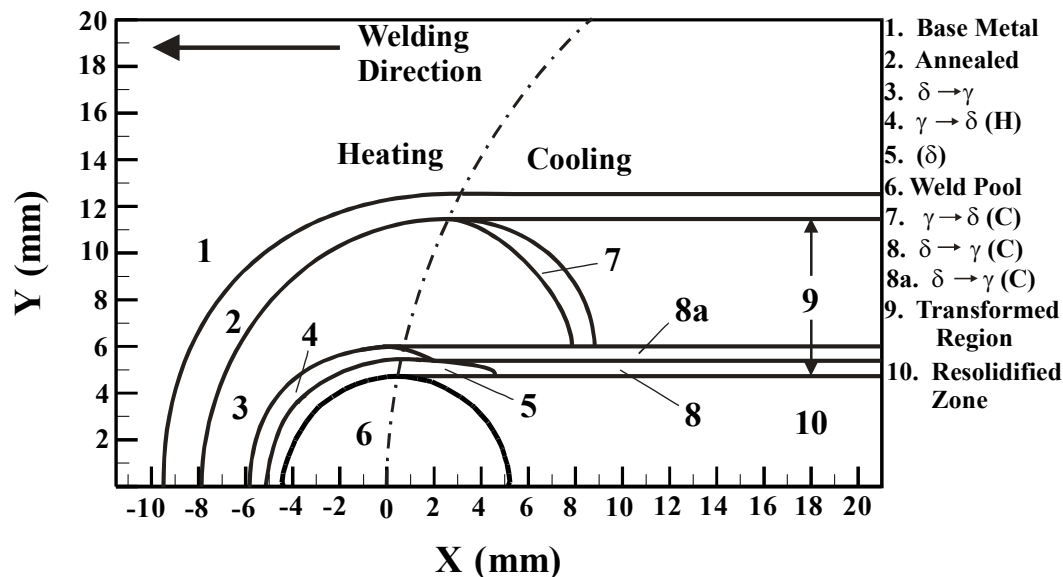


Figure 13. Schematic representation of HAZ phase transformation and annealing boundaries in the weldment determined from SRXRD data.

continues. Once the peak temperature is reached, the heating cycle is complete. However, several of the reactions dominant during heating (3-5) continue.

With the onset of cooling, another series of reactions become prevalent. With peak temperatures between approximately 700°C and 1100°C, the retransformation of γ back to δ occurs (7). This reaction matches the recovery in the ferrite volume fraction observed in Figure 10(b). The resulting δ/γ phase balance after the completion of this recovery is similar to that of the base metal. Even though the resulting microstructure resembles that of the base metal, this region has undergone a number of transformations and is identified as part of the transformed region (9). Regions with peak temperatures between 550°C and 700°C only undergo annealing during heating (2) and retain these characteristics during cooling to room temperature.

Regions near the weld pool (6) edge undergo a series of transformations different from those observed elsewhere. In regions where the γ phase is completely transformed δ (5), the δ phase undergoes a partial transformation to γ (8) on cooling. Only a small portion of the δ present in this region undergoes this transformation, leaving a δ/γ phase balance different from that in the base metal. A similar transformation occurs in the adjacent region (8a), where the partially transformed microstructure undergoes a partial transformation of δ back to γ . Unlike the transformation in region 8, which includes both the nucleation and growth of γ in a δ matrix, this $\delta \rightarrow \gamma$ phase transformation (8a) only involves the growth of existing γ grains. In both cases, the resulting δ/γ phase balance differs from that observed in the base metal. With the completion of these phase transformations, the final microstructure in the HAZ is formed.

Summary And Conclusions

A combination of *in-situ* SRXRD measurements and thermofluids modeling has been used to produce a map of the HAZ in a 2205 DSS weldment. The location and size of regions of completely transformed γ to δ , partially transformed γ to δ , and annealed δ and γ in the HAZ are identified. Based on these observations, conclusions regarding the real-time characteristics of the phase transformations occurring can be made.

A. A map showing the regions where the dominant phase transformations occur during both heating and cooling in the HAZ has been produced from a compilation of the SRXRD analyses (Figure 13).

B. A semi-quantitative map (Figure 9) of the δ/γ phase balance in the HAZ is developed from analysis of each SRXRD pattern. According to this map, the regions adjacent to the weld pool are completely transformed to δ during heating. With increasing distance from the weld pool, the δ volume fraction generally decreases. However, this decrease is not monotonic, and the δ content drops below that of the base metal in places.

C. A decrease in the δ volume fraction below the base metal value on heating followed by its recovery during

cooling is observed along a path parallel to the welding direction (Figure 10(b)) in region 3 of Figure 13. These transformations are predicted by thermodynamic calculations (Figure 3), but this work represents the first time these transformations have been directly observed.

D. A boundary between the annealed material and the base metal (Figure 12) is determined using FWHM measurements. This boundary corresponds with the calculated 550°C isotherm during the heating cycle and is unaffected by the cooling cycle.

Overall, this work provides an in-depth definition of the phase transformations occurring within the HAZ of a DSS weld. These observations have been possible only through the use of this novel observation technique (SRXRD) and lay the groundwork for a more detailed study of the kinetics of the δ/γ phase transformation in the HAZ during arc welding.

Acknowledgments

This work was performed under the auspices of the U.S. Department of Energy (DOE), Lawrence Livermore National Laboratory (LLNL), under Contract No. W-7405-ENG-48. The synchrotron experiments were performed at SSRL, which is supported by DOE, Division of Chemical Science. The authors would also like to thank Dr. S.S. Babu (Oak Ridge National Laboratory), Dr. T. DebRoy (The Pennsylvania State University), Mr. R. Kershaw (LLNL), and Mr. A.T. Teruya (LLNL).

References

1. *Metals Handbook: Properties and Selection: Iron, Steels, and High Performance Alloys*, 10th edn., Vol. 1, p 841, ASM International, Materials Park, OH, (1990)
2. J.-O. Nilsson, *Mater. Sci. Tech.*, 8, 685-700 (1992)
3. J.R. Davis (Ed.): *ASM Specialty Handbook: Stainless Steels*, p 340; ASM International, Materials Park, OH (1994)
4. D.J. Kotecki, in *Proc. 'First United States-Japan Symposium on Advances in Welding Metallurgy'*, San Francisco, CA, , American Welding Society, p 382 (1990)
5. T. Kitada, in *Proc. 'First United States-Japan Symposium on Advances in Welding Metallurgy'*, San Francisco, CA, June, American Welding Society, p 439 (1990)
6. T. Ogawa, T. Koseki, and H. Inoue: in *Weldability of Materials*, p 135, ASM International, Materials Park, OH (1990)
7. J.C. Lippold, I. Varol, and W.A. Baeslack: in *Duplex Stainless Steels*, p 383, Les Ulis Cedex; France (1991)
8. H. Hemmer and Ø. Grong, *Metall. Mater. Trans. A*, 30A, 2915-29 (1999)
9. H. Hemmer, Ø. Grong, and S. Klokkehaug, *Metall. Mater. Trans. A*, 31A, 1035-48 (2000)
10. S. Hertzman, P.J. Ferreira, and B. Brolund, *Metall. Mater. Trans. A*, 28A, 277-85 (1997)
11. S. Atamert and J.E. King, *Acta Metall. Mater.*, 39(3), 273-85 (1991)
12. S. Atamert and J.E. King, *Mater Sci. Tech.*, 8, 896-911 (1992)
13. P.D. Southwick and R.W.K. Honeycombe, *Metal Sci.*, 14, 253-61 (1980)

14. J.W. Elmer, Joe Wong, M. Fröba, P.A. Waide, and E.M. Larson: *Metall. Mater. Trans. A*, 27A, 775-83 (1996)
15. J.W. Elmer, Joe Wong, and T. Ressler, *Metall. Mater. Trans. A*, 29A, 2761-2773 (1998)
16. T. Ressler, Joe Wong, and J.W. Elmer, *J. Phys. Chem. B*, 102, 10724-10735 (1998)
17. Z. Yang, J.W. Elmer, J. Wong, and T. DebRoy, *Weld J.*, 79(4), 97s-111s (2000)
18. J.W. Elmer, Joe Wong, and T. Ressler, *Metall. Mater. Trans. A*, 32A, 1175-1188 (2001)
19. J.W. Elmer, Joe Wong, and T. Ressler, *Scripta Mater.*, 43(8) 751-757 (2000)
20. J.W. Elmer, Joe Wong, and T. Ressler, in *Joining of Advanced Specialty Materials II*, p 200, ASM International, Materials Park, OH (2000)
21. S.S. Babu, J.W. Elmer, S.A. David, and M. Quintana, unpublished research, 2001.
22. Designation A923-98, *Annual Book of ASTM Standards*, vol. 01.03, p 501, American Society for Testing and Materials West Conshohocken, PA (1998)
23. V. Karpenko, J.H. Kinney, S. Kulkarni, K. Neufeld, C. Poppe, K.G. Tirsell, J. Wong, J. Cerino, T. Troxel, J. Yang, E. Hoyer, M. Green, D. Humpries, S. Marks, and D. Plate, *Rev. Sci. Instrum.*, 60, 1451-1460 (1989)
24. *PowderCell*, v. 1.0, Federal Institute for Materials Research and Testing, Rudower Chaussee 5, 12489 Berlin, Germany
25. S.S. Babu: Private Communication, 2000.
26. S.A. David and T. DebRoy, *Science*, 257, 497-502 (1992)
27. T. DebRoy and S.A. David, *Rev. Mod. Phys.*, 67(1), 85-112 (1995)
28. K. Mundra, T. DebRoy, and K.M. Kelkar, *Numer. Heat Trans. A*, 29, 115-129 (1996)
29. Z. Yang and T. DebRoy, *Metall. Mater. Trans. B*, 30B, 483-493 (1999)
30. Z. Yang, *Modeling Weldment Macro and Microstructure from Fundamentals of Transport Phenomena and Phase Transformation Theory*, Ph.D. Thesis, The Pennsylvania State University, 2000.
31. W. Pitscheneder, T. DebRoy, K. Mundra, and R. Ebner, *Weld. J.*, 75(3), 71s-80s (1996)
32. E.A. Brandes (Ed.), *Smithells Metals Reference Book*, Seventh Edition, Butterworth and Heinemann, London, (1992)
33. M.W. Chase, Jr., C.A. Davies, J.R. Downey, Jr., D.J. Frurip, R.A. McDonald, And A.N. Syverud, *JANAF Thermochemical Tables*, 3rd Ed., American Chemical Society and American institute for Physics, Washington, DC, (1985)
34. S.S. Babu, Private Communication, 2000.
35. P. Sahoo and T. DebRoy, *Metall. Trans. B*, 18B, 597-601 (1987)
36. C. Limmaneevichitr and S. Kou, *Weld. J.*, 79(11), 324s-330s (2000)